6.3 A Multi-Scale Model of Helium Transport and Fate in Irradiated Tempered Martensitic Steels and Nanostructured Ferritic Alloys –

T. Yamamoto, G.R. Odette (Department of Mechanical Engineering, University of California Santa Barbara), R.J. Kurtz (Materials Science Division, Pacific Northwest National Laboratory) and B.D. Wirth (University of Tennessee, Knoxville)

OBJECTIVE

The synergistic effects of displacement damage and He produced by high energy neutrons in the fusion reactor environment can cause severe degradation of structural materials. The objective of this research is to develop a multiscale modeling tool for exploring the transport and fate of He under fusion relevant irradiation conditions. The model development is coordinated with well-designed in situ He implanter (ISHI) experiments in HFIR that enable characterization of microstructural evolution under the simultaneous introduction of both displacement damage and He at fusion reactor relevant He/dpa ratios. This report describes the master multiscale modeling framework, as well as some details of the sub-models and comparison of model predictions with experimental observables from recent ISHI experiments.

SUMMARY

Development and application of a multiscale model of the transport and fate of He in irradiated nanostructured ferritic alloys and tempered martensitic steels are described. Model predictions for He bubble average size, size distribution and number density are in reasonably good agreement with recent observations in ISHI experiments on F82H mod.3, 12YWT and MA957.

PROGRESS AND STATUS

Introduction

One of the challenges that fusion reactor materials development faces is to predict and mitigate the effects of transmutation He on the mechanical properties of first wall structural materials. In a typical DEMO fusion reactor design, after a year of operation at a neutron wall load of 5 $MW/m^2 \approx 500$ appm He will be generated in Fe-based materials, as well as displacement damage doses of ≈ 50 dpa. Helium bubbles form in the matrix as well as on dislocations, precipitate interfaces and grain boundaries (GB) [1]. Based on a physically motivated analysis of limited data in the literature for fracture toughness transition temperature shifts (ΔT), we previously proposed a model that predicts that irradiation hardening ($\Delta\sigma_y$) coupled with GB He embrittlement of tempered martensitic steels (TMS) produces very large ΔT at low irradiation temperatures [2,3]. Our previous predictions are in remarkably good quantitative agreement with recent spallation proton irradiation data, showing extraordinary ΔT up to > 500ºC in TMS containing ≈ 2000 appm He at ≈ 20 dpa [4]. The synergistic effects of irradiation hardening and GB He embrittlement appears to emerge at He levels > ≈500 appm corresponding to one year of operation at high wall loading. There is also a transition from transgranular cleavage to intergranular fracture [2,3]. The spallation proton data also show that high levels of He extend the range of large ΔT to above 400°C. At high irradiation temperatures matrix He may promote void swelling and He accumulation on GBs could also severely degrade creep rupture and related properties. These observations and models suggest that the temperature window for using TMS in DEMO reactor applications may be significantly narrower than previously believed, and may even close. Thus a major challenge will be to design and develop an new class of nanostructured ferritic alloys (NFA), that are dispersion strengthened by an ultra high density of Y-Ti-O enriched nanometer-scale features (NF), that can protect GBs and prevent swelling by trapping He in very small bubbles at NF interfaces [5-7]. The objective of the present research is to develop a tool to predict material performance, as a function of material and environmental variables such as microstructure, chemical composition, displacement damage (dpa), He/dpa ratio and temperature. In this report we describe the development and application of a multiscale model of the transport and fate of He in irradiated NFAs and TMS.

Multi-scale Modeling

The model was built by considering the multiscale nature of the phenomena, both in time and length scales. Key elements of the basic interactions of He atoms with various features in the material microstructure as well as He migration have been atomistically modeled using molecular statics (MS), molecular dynamics (MD) and kinetic Monte Carlo (kMC) simulations. The MS simulations included the Dimer method to determine defect migration saddle point energies. Details of the atomistic models are described elsewhere [8-17]. Briefly, the interaction of He atoms, vacancies, and He-vacancy clusters with key microstructural features such as dislocations, NFs and GBs were modeled and information such as binding and migration energies were incorporated in the modified rate theory (MRT) differential equations. In some cases a type of energy (e.g. interstitial He to GB binding energy) depended on GB character [9,10,13-15]. For the calculations reported here the MRT integration code used a representative single value. Parametric studies are being performed to test the sensitivity of the model to the values we selected.

Current Integration Model Structure

The model is specifically aimed at treating intermediate to high irradiation temperatures, which are outside the low-temperature displacement damage and defect cluster dominated regime, at least for low He conditions. Reaction rate theory is used to model the transport and interactions of point defects and He, as well as He clustering, which leads to bubble formation and growth. Figure 1 shows the framework of the model. He transport and interactions in the matrix and within microstructural subregions are separately treated according to the characteristics of each region. In the matrix, point defects recombine at precipitate trap sites as well as in the matrix, or diffuse to permanent sinks such as dislocations and GBs to produce steady state concentrations of vacancy (V) and self-interstitial atoms (SIA). Helium is generated by transmutation reactions in interstitial, He(i), or substitutional, He(s), forms. These can switch form by reacting with V and SIA as follows:

$$He(i) + V = He(s) \quad (1a)$$

$$He(s) + SIA = He(i) + [V+SIA\ recombination] \quad (1b)$$

The two forms of He atoms migrate at appropriate diffusivities until they meet other He atoms and Vs to create He_mV_n clusters in the matrix, or they reach sub-region sinks that are, in the current model, NF, dislocations and GBs. The He can be emitted as well as absorbed, hence He can recycle between various features and sub-regions they contain Bubble formation and evolution is modeled using a cluster dynamics algorithm. The concentration of clusters with i He atoms and the balanced number of vacancies, $C_{mxb}(i)$ ($i > 2$), is solved by a set of rate equations considering following reactions:

$$He(i) + He(s) + \langle V\rangle = H_2V_{n(m)} \quad (2a)$$

$$He(s) + He(s) + \langle V\rangle = H_2V_{n(m)} \quad (2b)$$

$$He_mV_{n(m)} + He(i) + \langle V\rangle = He_{m+1}V_{n(m+1)} \quad (2c)$$

$$He_mV_{n(m)} + He(s) + \langle V\rangle = He_{m+1}V_{n(m+1)} \quad (2d)$$

$$He_mV_{n(m)} = He_{m-1}V_{n(m-1)} + He(s) + \langle V\rangle \quad (2e)$$

Here, the $H_mV_{n(m)}$ clusters are all assumed to be stable bubbles with He gas pressure that balances the capillary pressure caused by surface tension. A hard sphere model is used for the equation of state (HSEOS), in terms of a master equation to relate ideal gas model radius to HSEOS real gas radius

developed by Stoller and Odette [18]. The master equation gives the relationship between the ideal to real gas radius ratio, $[r_{b,ideal}/r_{b,HSEOS}]$ as a function of a reduced radius, $R = r_{b,ideal}[kT/\gamma]^{1/3}$. Here, k is Boltzman's constant, T is the absolute temperature and γ is the free surface energy, typically ≈ 2.0 (J/m^2) for BCC Fe. For small He clusters (i < 20) the He/V ratio is between 1 to 1.3 in the temperature range from 500 to 600ºC. For these He/V ratios, the binding energy of He to the cluster is more than ≈ 2.5 eV according to ab inito calculations by Fu [19] and more than ≈ 4 eV in molecular dynamics calculations by Morishita et al. [20]. This suggests that, to first order, a two He atom cluster is a bubble nucleus. We plan to implement a stochastic nucleation model in the future.

He atoms captured by precipitates, dislocations, and GBs may be re-emitted back into the matrix at a rate dictated by the binding energy to that feature, or the feature subregion, the jump frequency, and the temperature. Alternately, He diffuses within the subregion until He + He reactions nucleate a bubble, or the mobile He joins He_mV_n bubbles. He atoms are also be trapped at lower energy sites within the subregion for a time that is again dictated by the binding energy. There is an increased chance of He + He -> heterogeneous bubble nucleation reaction at the low energy sites. Bubble also nucleate homogeneously on dislocation segments, in the matrix and at other features such as GB and precipitate interfaces, and bubbles that act as permanent He traps.

The local transport, trapping and interactions have been modeled according to the dimensional and energetic characteristics of the sub-region. For example, on dislocations diffusion of a He takes place one-dimensionally along the dislocation line between deeper trap sites such as bubbles, intersections and nm-scale precipitates, as shown in Figure 2a. At steady state the He concentration profile between trapping sites has a zero-gradient peak at the middle. Since there is no net He flow at the peak, the dislocation network can be represented by a distribution of isolated dislocation segments, with a trapping site at the center, as illustrated in Figure 2b. The segments are modeled as a distribution of length, L(k), where $1 \le k \le n_{seg}$, where n_{seg} is the number of unique segment lengths. For pre-existing traps, L(k) is assumed to have a log-normal distribution, with an average length <L>, that is determined by the total number of the trap sites and the dislocation density, ρ. The total number of pre-existing trap sites, N_{TS}, is taken as the sum of N_{IS} for dislocation intersections and N_{PD} for precipitates on dislocations. Assuming the spacing of trapping sites on individual dislocations is $\rho^{1/2}$ and $(2\, r_p\, N_p)^{1/2}$, N_{TS} is

$$N_{TS} = N_{IS} + N_{PD} = \rho^{3/2} + \rho\,(2\, r_p\, N_p)^{1/2} \qquad (3a)$$

The average segment length <L> is

$$\langle L \rangle = \rho / N_{TS} \qquad (3b)$$

For example, for a typical NFA with $N_P = 6.6\text{x}10^{23}/m^3$, $r_P = 1.5$ nm (or 1% volume fraction of precipitates, f_V) and $\rho = 10^{15}/m^2$, N_{IS} and N_{PD} are 3.2 and 4.6x $0^{22}/m^{-3}$, respectively, resulting in an average segment length <L> of 12.9 nm. The number density, N(k), of larger and smaller k-th segment, that are scaled as multiples of the Burger's vector b, is assumed to have a log normal distribution. Figure 2c shows an example of the N(k) distribution as a function of L(k) with distribution width parameter, $\beta_m = 0.4$. Reaction between trapped and mobile converts the site to a permanent bubble trap. Once formed the dislocation bubbles grow by collecting the He that diffuses along the dislocation segment lengths.

However, bubbles are permanent traps for He and also nucleate homogeneously in the various regions. In the case of dislocations, homogeneous bubble nucleation requires dynamic re-segmentation of the dislocation network length distribution. The reaction rate is taken to be the same as in the case of deep traps, except that the segment length is taken as L(k)/2 and the diffusion coefficient is doubled to $2D_{He(seg)}$. The initial segment is then partitioned into two segments with length classes of k_1 and k_2 depending on the original length class k. If k is an even number, then $k_1 = k_2 = k/2$. If k is an odd number, then

k_1=(k-1)/2 and k_2=(k+1)/2. All i He atoms at the trap are assigned to the k_1 class segment to make a segment (i,k_1), and the new nucleus is assigned to a (2, k_2) segment.

The new segments containing homogeneously nucleated He bubbles are treated site holding two He atoms in the k_2 length class. The $C_{He}^{seg(i,k)}$ on the original segment is evenly added to those of the two new segment classes, $C_{He}^{seg(i,k1)}$ and $C_{He}^{seg(2,k2)}$. The reason why the segment lengths were modeled to have a fixed multiple (M) Butger's vector unit length, L_u = Mb, is because it enables segment division without generating a new segment class that would have a different length from any existing segment class.

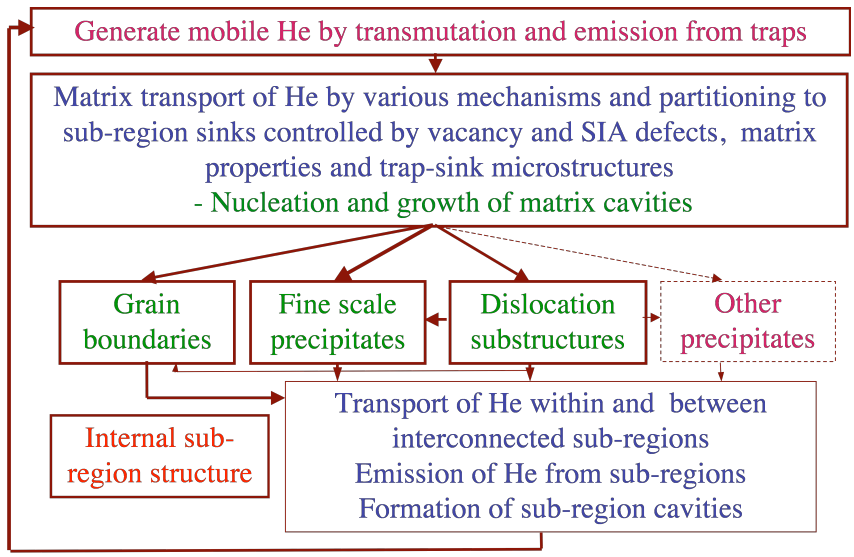

Figure 1 Master model framework showing the regions considered in the model as well as He transport between the regions.

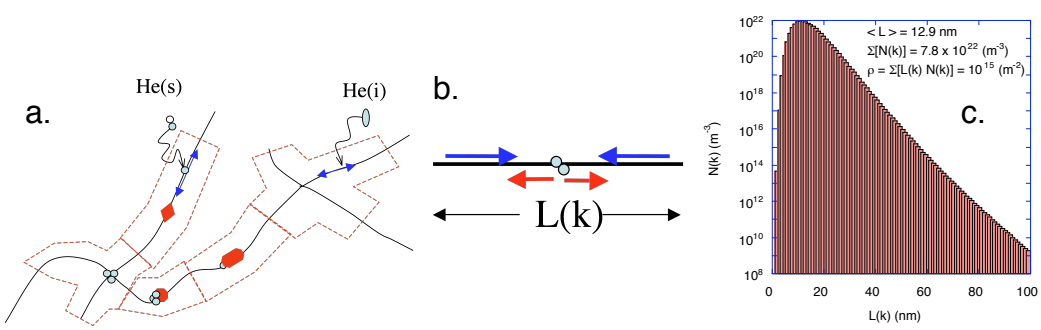

Figure 2 (a) A schematic dislocation network having intersections and precipitates as deeper He trap sites, (b) the simplest model of a part isolated at the middle points between any two of the deeper sites and (c) a modeled log-normal type distribution of the segment length with β_m = 0.4.

The rate at which He atoms on a dislocation segment are captured at the trap site is obtained by solving the one-dimensional steady-state diffusion Equation 4a. This assumes immediate capture at the surface of the trap site at x=r_o so that He generation (or capture from the matrix), G_{He}, per unit length is uniform over the entire segment and should balance the net transfer of He from any location on the segment towards the trap site. Solving Equation 4a with boundary conditions shown in Equation 4b gives a

general solution shown in Equation 4c. The red solid curve in Figure 3 is an example a $C_{He}(x)$ solution for the case of a segment length of 12.9 (nm) and a capture radius of r_o = b = 0.248 (nm). The dashed blue line shows the average He concentration over the entire segment length, $<C_{He}>$, which is generally given by Equation 4d. The transfer rate S_{DT} defined in $D_{He}S_{DT}<C_{He}> = G_{He}$ is given by Equation 4e.

$$D_{He}\, d^2C(x)/dx^2 + G_{He} \text{ (capture from the matrix)} = 0 \qquad (4a)$$

$$C(x) = 0 \text{ at } x = r_o;\ dC(x)/dx = 0 \text{ at } x = L/2 \qquad (4b)$$

$$C_{He}(x) = (G_{He}\, L^2 / 2\, D_{He})\ \{ (x/L - r_o/L) - (x^2/L^2 - r_o^2/L^2) \} \qquad (4c)$$

$$< C_{He} > = (G_{He}\, L^2 / 2\, D_{He})\ (1/6 - r_o/L + 2\, r_o^2/L^2 - 4/3\, r_o^3/L^3) \qquad (4d)$$

$$S_{DT} = G_{He} / D_{He} < C_{He} > = 1 / \{L2\ (1/12 - r_o/2L + (r_o/L)^2\} \qquad (4e)$$

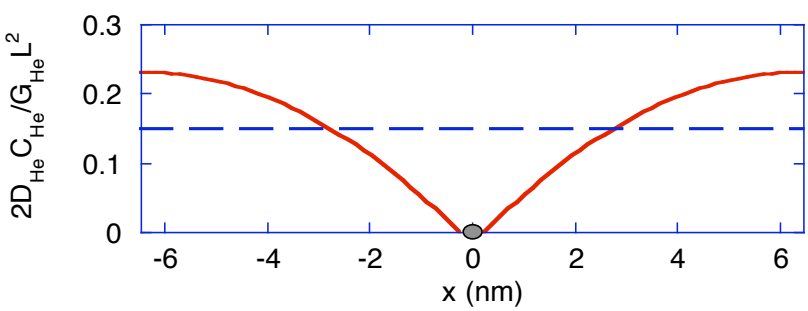

Figure 3 A steady-state He concentration profile (red solid line) on a dislocation segment with L = 12.9 (nm) for a uniform He generation G_{He} and capturing at a site of radius, r_o (nm), at diffusion coefficient D_{He}. Blue dashed line shows the average He concentration $<C_{He}>$ over the entire segment.

A cluster dynamics approach is also applied to model bubble evolution on dislocation segments. For every segment length class, k, the concentration of segments holding i He atoms in the trap site, $C_{seg(i,k)}$ (i = 0 to n_{max}), and the concentration of untrapped He atoms (shown as the shaded regions in Figure 4), $C_{He}^{seg(i,k)}$, are modeled by a set of ordinary differential equations. The general forms for $dC_{seg(i,k)}/dt$ and $dC_{He}^{seg(i,k)}/dt$ are given by Equations 5a and 5b, respectively. Here, $S^s_{is(i,k)}$ is the sink strength of the trap site for the untrapped He concentration, $C_{He}^{seg(i,k)}$, in the segment, and $D^{seg}_{He(s)}$ is the diffusion coefficient of He atoms along dislocations. Equation 5a also considers He atom emission from the trap at a rate β^s_{is} given by Equation 5c, where $E_b{}^s_{is}$ is the binding energy of the He(s) atom to the trap site. Note that the current model allows emission of He only for i < 2. As has been stated previously the $He_2V_{n(2)}$ cluster is taken to be a stable bubble. A more accurate treatment of He emission from small He clusters will be included in future versions of the model. The first and second term in the Equation 5baccount for He(s) or He(i) captured by the segment from the matrix, which depends on the dislocation density, and emission of He from all segment regions to the matrix at a rate β^s_{disl}, given in Equation 5d. The third and fourth terms account for the transfer of the previous segment to another segment class by the trap site capturing or emitting He. An integer number, $n_{He}^{seg(i,k)}$, is used to account for the number of He atoms that are being carried by the segment. The $n_{He}^{seg(i,k)}$ is taken as the $C_{He}^{seg(i,k)}/C_{seg(i,k)}$ ratio, rounded up to the nearest integer number for capture, since reactions are more likely on a segment carrying more He atoms than average, while the ratio rounded down for emission.

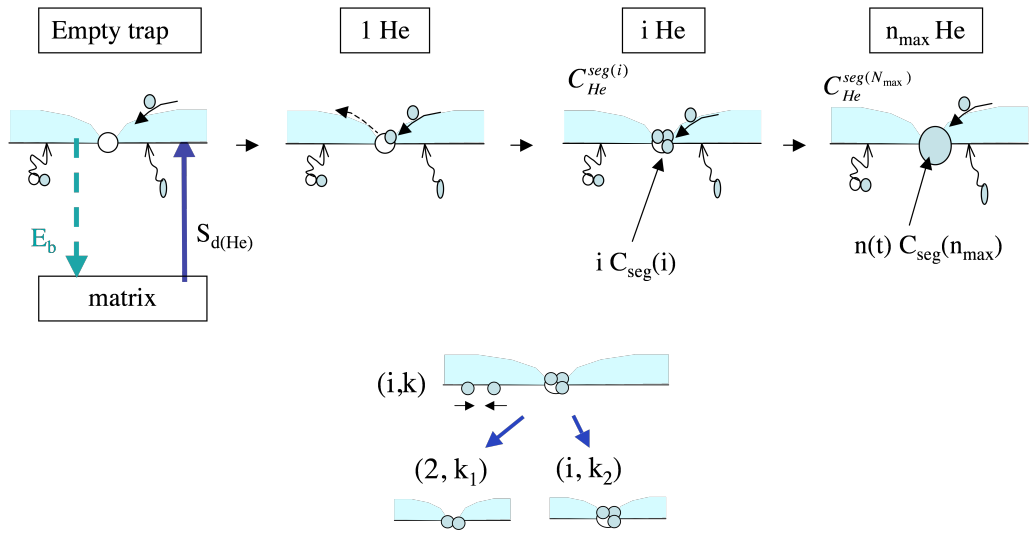

Figure 4 Schematics of a CD algorithm for He cluster formation at a trap site on a dislocation segment with a length $L(k)=kL_U$ (top) and for a treatment of homogeneous cluster nucleation other than the trap site (bottom).

$$dC_{seg(i,k)}/dt = S^{s}_{is(i-1,k)} D^{seg}_{He(s)} C^{seg(i-1,k)}_{He} - S^{s}_{is(i,k)} D^{seg}_{He(s)} C^{seg(i,k)}_{He} + \beta^{seg(i+1,k)}_{is}\left[(i+1)\cdot C_{seg(i+1,k)}\right] - \beta^{seg(i,k)}_{is}\left(i\cdot C_{seg(i,k)}\right) \tag{5a}$$

$$dC^{seg(i,k)}_{He}/dt = \left(S^{h}_{disl} D_{He(i)} C_{He(i)} + S^{s}_{disl} D_{He(s)} C_{He(s)}\right) C_{seg(i,k)} L(k)/\rho\Omega - \beta^{s}_{disl} C^{seg(i,k)}_{He} + S^{s}_{is(i-1,k)} D^{seg}_{He(s)} C^{seg(i-1,k)}_{He}\left(n^{seg(i-1,k)}_{He} - 1\right) - S^{s}_{is(i,k)} D^{seg}_{He(s)} C^{seg(i,k)}_{He}\left(n^{seg(i,k)}_{He} - 1\right) + \beta^{seg(i+1,k)}_{is}\left[(i+1)\cdot C_{seg(i+1,k)}\right]\left(n^{seg(i+1,k)}_{He} + 1\right) - \beta^{seg(i,k)}_{is}\left(i\cdot C_{seg(i,k)}\right)\left(n^{seg(i,k)}_{He} + 1\right) \tag{5b}$$

$$\beta^{seg(i,k)}_{is} = D^{seg}_{He(s)} \exp\left(-E^{s}_{b\,is}/kT\right)/b^2 \tag{5c}$$

$$\beta^{s}_{disl} = D^{mtx}_{He(s)} \exp\left(-E^{s}_{b\,disl}/kT\right)/b^2 \tag{5d}$$

$$dC^{nucl}_{seg(i,k)}/dt = -S^{s,nucl}_{is(i,k)} 2 D^{seg}_{He(s)} C^{seg(i,k)}_{He}\left[C^{seg(i,k)}_{He}/C_{seg(i,k)}\right] \tag{5e}$$

As noted previously, bubbles also homogeneously nucleate by He + He reactions on dislocation segments. The rate of nucleation is given by Equation 5e.

The original $C_{He}^{seg(i,k)}$ on segment before a new bubble nucleates is evenly divided between the two new segments. Homogeneously nucleated bubbles also grow by the diffusion of He along the dislocation segments as well as He fluxes from the matrix in the same way as bubbles formed on traps.

He bubble formation in GBs is modeled similarly accounting for both the trap site and homogeneous nucleation mechanisms. The entire GB area is divided into circular regions with area, A_{trap}, for each trap site. The concentration, $C_{gt}(i)$, carrying i He atoms is tracked using the cluster dynamics method for two-dimensional He diffusion in A_{trap}. For simplicity, homogeneously nucleated $He_2V_{n(2)}$ clusters are combined with the $C_{gt}(2)$ trap formed He bubble nuclei class. The A_{trap} is updated based on the total number of the

trap sites, including new homogeneously nucleated bubbles. Flow of He atoms in a GB to the trap site is found by solving the two dimensional diffusion equation, analogous to that for He fluxes from the matrix to dislocations. This involves replacing the dislocation density with $1/A_{trap}$ and the core radius with the trap site (or bubble) radius. The governing equations are given by:

$$S^{s}_{GBT(i)} = /\ln[R_{trap}/r(i)]\left(1/A_{trap}\right) \tag{6a}$$

$$\begin{aligned} dC_{GBT(i)}/dt = {} & S^{s}_{GBT(i-1)}D^{GB}_{He(s)}C^{GB}_{He} - S^{s}_{GBT(i)}D^{GB}_{He(s)}C^{GB}_{He} \\ & + \beta^{s}_{GBT}\left[(i+1)C_{GBT(i+1)}\right] - \beta^{s}_{GBT}\left(i \cdot C_{GBT(i)}\right) \end{aligned} \tag{6b}$$

$$\beta^{s}_{GBT} = D^{GB}_{He(s)}\exp\left(-E^{s}_{bGBT}/kT\right)/b^{2} \tag{6c}$$

He cluster formation on NFs have been also modeled by cluster dynamics algorithm. In the current version of the model each NF has a maximum of one bubble with i He atoms, Helium is trapped on and emitted from the NFs at a rate specified by a binding energy $E_{bnf}^{He(s)}$. Bubble nucleation is treated by assuming that a second He atom reaching a NF with a previously trapped He atom immediately forms a bubble. Vacancies and interstitials are also trapped at NFs, which also act as recombination centers. NFs trap He and point defects by three dimensional diffusion mediated by the matrix composition of and the NF-bubble sink strength given by,

$$S^{s}_{NF(j)} = 4\pi r_{NF(j)}C_{NF(j)}\left(1 + r_{NF(j)}\sqrt{S_t}\right)/\Omega \tag{7a}$$

$$\begin{aligned} dC_{NF(j)}/dt = {} & S^{s,h}_{NF(j-1)}\left(D_{He(i)}C_{He(i)} + D_{He(s)}C_{He(s)}\right) - S^{s,h}_{NF(j)}\left(D_{He(i)}C_{He(i)} + D_{He(s)}C_{He(s)}\right) \\ & + \beta^{s}_{NF(j+1)}C_{NF(j+1)} - \beta^{s}_{NF(j)}C_{NF(j)} \end{aligned} \tag{7b}$$

$$\beta^{s}_{NF(j)} = D^{mtx}_{He(s)}\exp\left(-E^{s}_{bNF(j)}/kT\right)/b^{2} \tag{7c}$$

The preceding thumbnail sketch of the model does not include all the details of the formulation of the complex code containing 3000 to 8000 equations, that will be further described in future reports.

Companion HFIR Experiments using He-implanter Technique

The model calculations are compared with our systematically designed and carefully controlled experiments in the HFIR, a mixed spectrum reactor. While the details are given elsewhere [5-7,21-23], the so-called in-situ He-implantation (ISHI) experiments utilize NiAl coating that is deposited on TEM samples of TMS, NFA and model Fe-based alloys. The isotope, ^{58}Ni, which is about 60% of the natural Ni in the NiAl coating reacts with thermal neutrons to emit He as α-particles with 4.71 MeV energy. Depending on the thickness of the coating, He is implanted uniformly over an ≈ 6 to 8 μm thick layer from the sample surface adjacent to the coating. The He-to-dpa ratio ranges from ≈ 5 to 50 appm He/dpa, depending on the coating thickness. Our recent results clearly showed differences in He precipitation behavior between TMS alloys F82H and Eurofer versus NFA MA957 and 12YWT[5-7,22-23].

Model calculations have been performed for the typical TMS and NFA microstructural parameters shown in Table 1. The corresponding values of the thermodynamic parameters used in the model are shown in Table 2. The examples shown here are for a He/dpa ratio of 40 at 500°C and a dpa rate of 10^{-6} dpa/s

Table 1 Microstructural Parameters

Model	ρ (m^{-2})	Grain size	Sink strength (m^{-2})		
			NF	Dislocation	GB
TMS-1	3×10^{14}	20 μm	-	$\approx 10^{14}$	$\approx 10^{13}$
TMS-2	1×10^{15}	20 μm	-	$\approx 10^{15}$	$\approx 10^{13}$
TMS-3	1×10^{15}	2 μm	-	$\approx 10^{15}$	$\approx 10^{14}$
NFA-1	1×10^{15}	20 μm	$\approx 10^{16}$	$\approx 10^{15}$	$\approx 10^{13}$
NFA-2	1×10^{15}	2 μm	$\approx 10^{16}$	$\approx 10^{15}$	$\approx 10^{14}$

Table 2 Model Thermodynamic Parameters

Parameter		Value
Binding energy of He (s)	To dislocations (disl.)	0.9 eV
	To nm-scale features (NF)	0.59 eV
	To grain boundary (GB)	0.5 eV
	To disl. Intersection vs. disl.	0.6 eV
	To NF on disl. vs. disl.	0.6 eV
	To deep trap on GB vs. GB	0.6 eV
Binding energy of V	To NF	0.6 eV
Migration energy of	He(i) in matrix	0.08 eV
	He(s) in matrix	2.35 eV
	V in matrix	1.40 eV
	SIA in matrix	0.08 eV
	He(s) on dislocations	1.18 eV
	He(s) on GB	1.18 eV
Formation energy of	Vacancy	1.6 eV

Results and Discussion

Bubble nucleation of dislocations accompanied by division of the segments

The model predicts that dislocations play a dominant role in bubble formation. Figure 5a shows an example of the change in the dislocation segment length distribution as a function of dpa for the TMS model. The change in the distribution to a larger number of shorter segments becomes significant above about 10^{-3} dpa. Figure 5b shows the total number of segments, the number of segments carrying bubbles and the number of homogeneously nucleated bubbles plotted as a function of dpa for both the TMS and NFA models. In the TMS case, most of the bubbles nucleated homogenously on dislocations at damage levels less than ≈ 0.01 dpa. The increase in the number of segments corresponds to the number of homogeneously nucleated bubbles. The number of segments increases by a factor of ≈ 3 saturating at ≈ 0.2 dpa. The bubbles formed by heterogeneous nucleation at a trap sites are reflected by the difference between the total bubble number density and of the number density of homogeneouly nucleated bubbles,

which becomes moderately significant above ≈ 0.01 dpa. Figure 5c shows the bubble nucleation rates plotted as a function of dpa. Clearly, homogeneous nucleation is the dominant mechanism for bubble formation on dislocations. As shown in Figures 5b and d, similar behavior is observed in the NFA. However, in this case the dpa are shifted up by about an order of magnitude than for the TMS, and bubble nucleation continues up to several dpa. The delay in the dislocation bubble formation in NFA is largely due to the effect of He trapping by NFs, which are described in more detail in the following section.

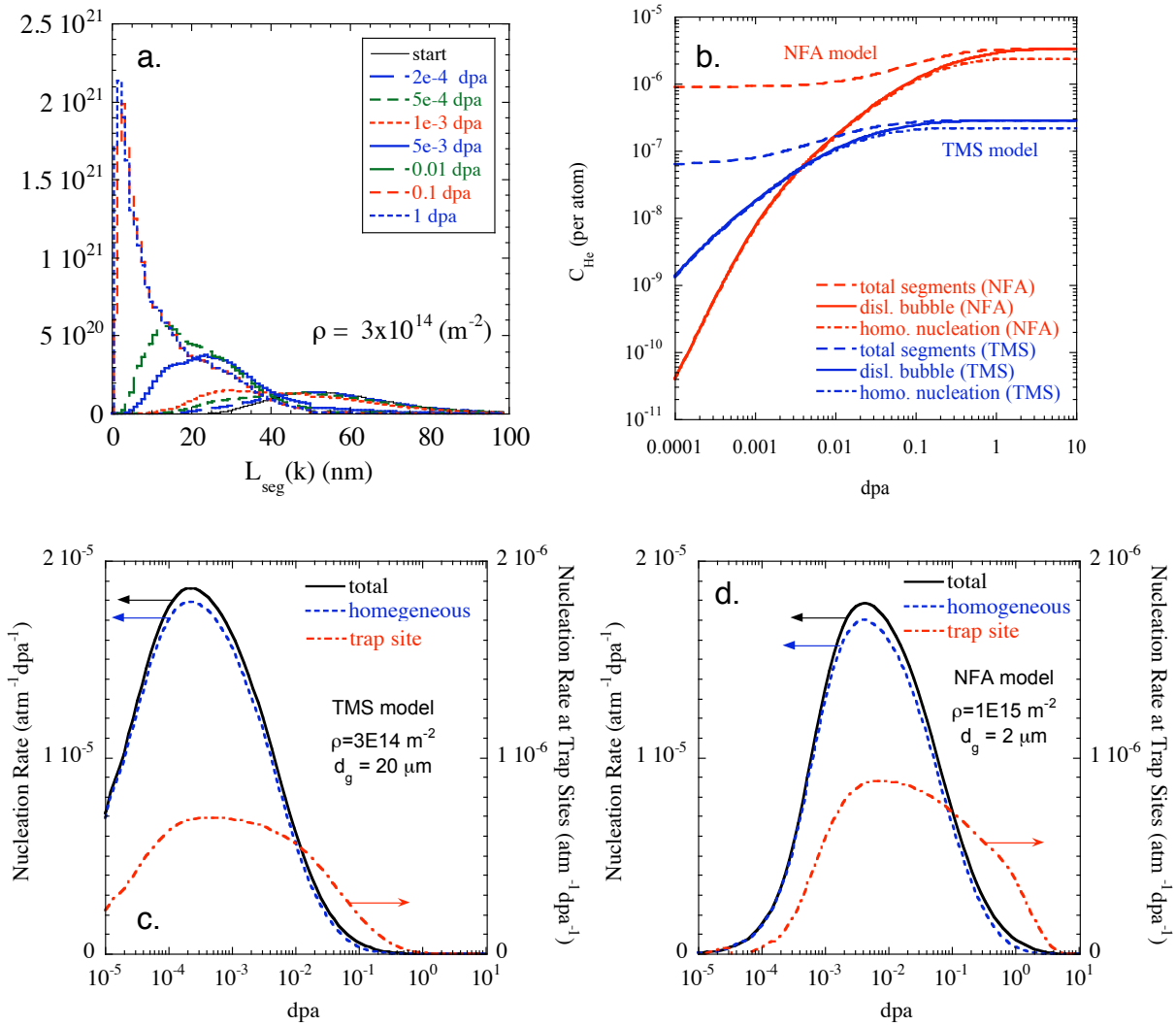

Figure 5 (a) Evolution of the dislocation segment length distribution, through 1 dpa of neutron irradiation with He generation at 10 appm He/dpa, in a TMS model with dislocation density of 3 x 10^{14} (m^{-2}), and (b) total number density of dislocation segments as well as that of He cluster carrying segments for both of TMS (ρ = 3 x 10^{14} m^{-2}) and NFA (ρ = 1 x 10^{15} m^{-2}) models.

He partitioning and bubble formation in the TMS models

Figure 6 shows He partitioning into subregions, represented in terms of both the He concentration per total number of atoms (Figure 6a, c, e) as well as per the number of atoms in the subregion (Figure 6b, e, f), which we refer to as "coverage" below, for TMS models with various dislocation densities (ρ) and grain diameters (d_g). Figures 6a-b, c-d and e-f show the results for ρ=3x10^{14} m^{-2} and d_g = 20 μm, ρ = 10^{15} m^{-2}

and d_g = 20 μm, and ρ=10^{15} m^{-2} and d_g = 2 μm, respectively. For this range of parameters, the He largely partitions to dislocations. Starting at a dose and He level lower than 10^{-5} dpa and 4 x 10^{-4} appm He, essentially all of the He partitions to dislocations, as shown by the red sold lines in Figures 6a, c, e. Most the He is in the form of single atoms spread over dislocation segments up to a dose of ≈ 2 x 10^{-5} and 5 x 10^{-5} dpa, respectively, for ρ = 3 x 10^{14} m^{-2} and ρ = 10^{15} m^{-2}. Dislocation bubbles nucleate both homogeneously and heterogeneously at higher doses. Both the He_s and He_i reach a quasi-steady state concentration after ≈ 10^{-5} dpa at ≈10^{-10} and 10^{-20}, respectively.

Matrix bubble nucleate at a low rate by He_s + He_s reactions. In rough proportion the total He in both cases. Hei is immediately partitioned to all the subregions and bubble sites. He partitioning to GBs is strongly affected by grain size. In the case of d_g = 20 μm, the partitioning to GBs is roughly constant up to ≈ 0.01 dpa, followed by a gradual increase. For the d_g = 2 μm case, He partitioning increases more rapidly above 10^{-4} dpa, so that about 10^3 times more He accumulates at GBs than for the case with d_g = 20 μm. As shown below in the bubble size and number density trends, the rapid increase in partitioning to GB is due to by bubble nucleation and growth as early as 0.001 dpa for the case with d_g = 2 μm, due to the fact that bubbles are permanent traps for He. The resulting saturation GB He coverage are ≈ 10^{-7} and ≈ 10^{-5} for d_g = 20 μm and d_g = 2 μm, respectively.

Figure 7 summarizes the number density and average size (radius) of the bubbles in each sub-region as a function of dpa for all the TMS models. The plots also include the measurements from He implanter experiments performed for F82H mod.3 in both the as tempered and 20% cold worked conditions. The bubble number density and average size in the model for low and high dislocation density shows reasonably good agreement with the experimental data obtained for both of these conditions. The dominance of bubble nucleation on dislocations predicted by the model is also consistent with experimental observations.

While the overall agreement between model and experiment is reasonably good, GB He bubble formation in the model somewhat underestimates the bubble formation observed on lath boundaries in the experiments. Changing the grain size in the model to the experimental lath size was a first-order approximation that demonstrated that the GB bubbles start forming and growing at very low dose. The 10^{-5} He coverage corresponds to one bubble containing ≈ 10 He atoms (r_b = 0.3 nm) in every ≈ 4x10^4 nm^2. The bubble density on boundaries have not been quantified, but appears to be qualitatively larger than the model predictions. The predicted size of the bubbles is smaller than those that are observed. Future refinements of our model will include more appropriate treatment of the lath boundaries.

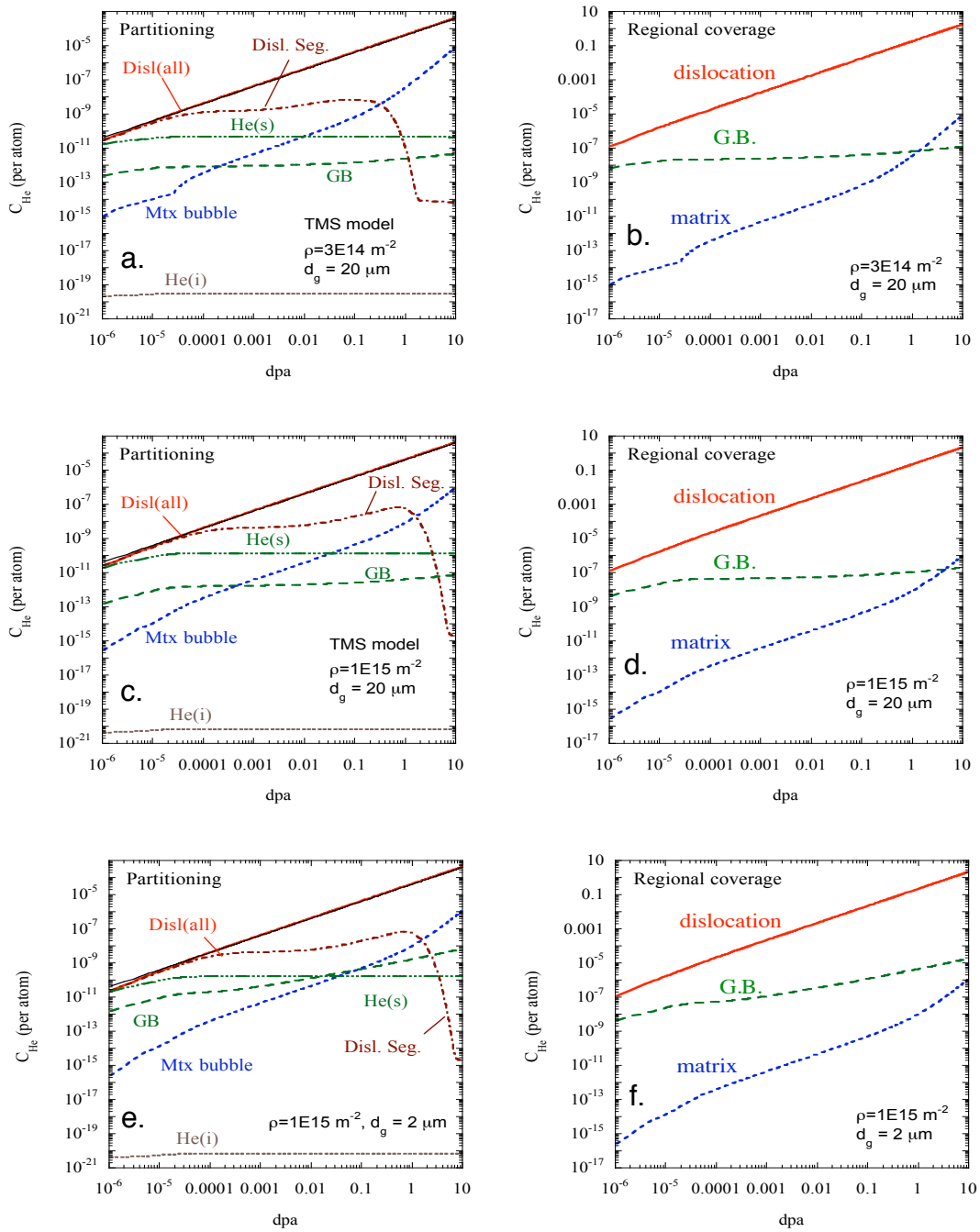

Figure 6 He partitioning into subregions, in terms of He concentration per total atoms ((a), (c) and (e)) as well as per subregion atoms ((b), (e), and (f)), refered as "coverage", for TMS models with various dislocation densities (ρ) and grain diameters (d_g). (a) and (b) for ρ=3x10^{14} m^{-2} and d_g = 20 μm, (c) and (d) for ρ = 10^{15} m^{-2} and d_g = 20 μm, and (e) and (f) for ρ=10^{15} m^{-2} and d_g = 2 μm.

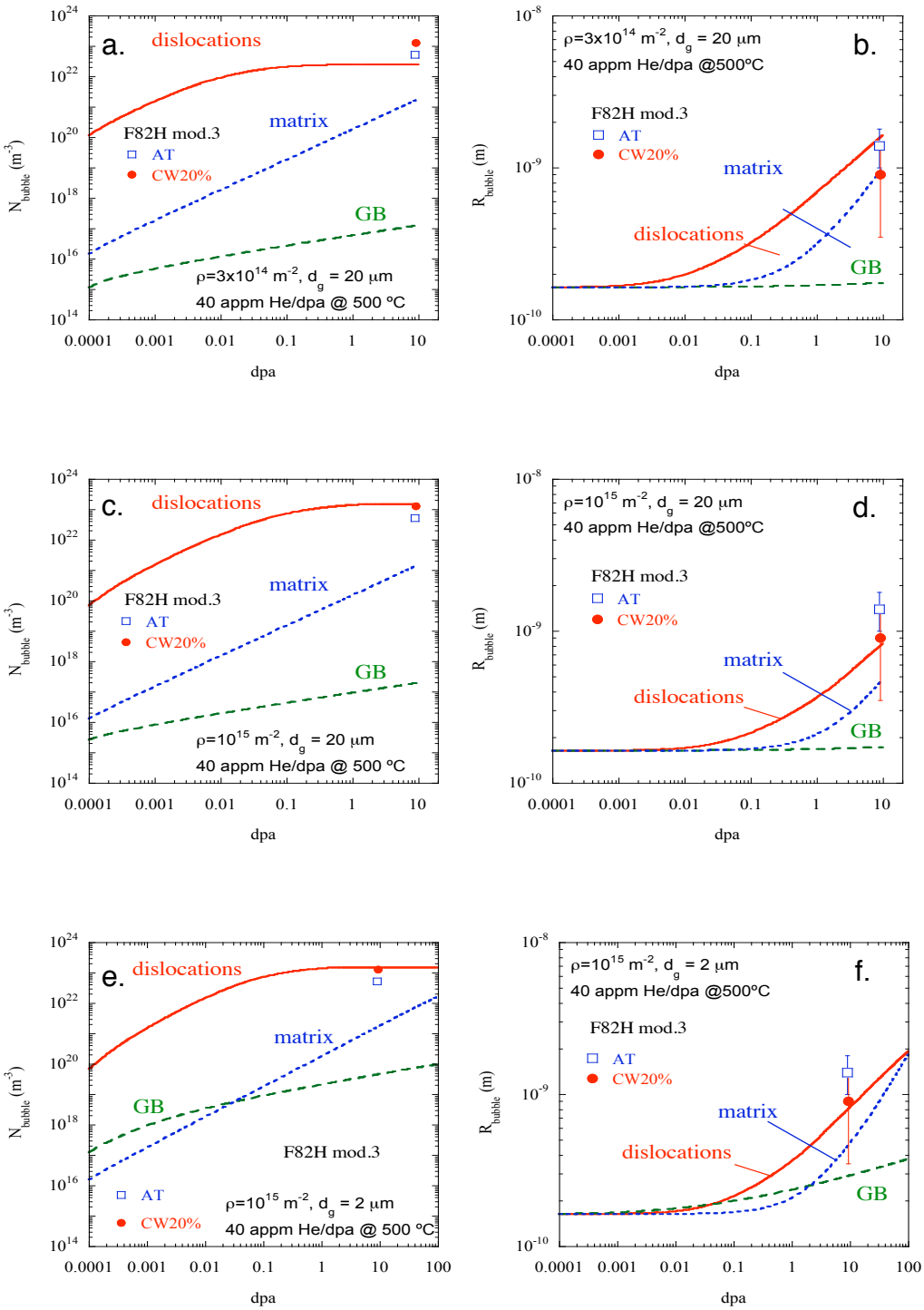

Figure 7 He bubble number density and average size (radius) in various sub-regions as a function of dpa for TMS models with various dislocation densities (ρ) and grain diameters (d_g). (a) and (b) for $\rho=3\times10^{14}$ m^{-2} and d_g = 20 μm, (c) and (d) for $\rho = 10^{15}$ m^{-2} and d_g = 20 μm, and (e) and (f) for $\rho=10^{15}$ m^{-2} and d_g = 2 μm, compared with the observation in He-implanter experiments on F82H mod.3 at as-tempered (AT) and 20% cold worked (CW20%) conditions.

He partitioning and bubble formation in the NFA models

Figure 8 shows He partitioning to and coverage of sub-regions in NFA models. Figures 8a-b and 8c-d are for coarse (20μm) and fine (2μm) grain size cases, respectively. The same NF size (radius), r_{NF} = 1.5 nm and number density, N_{NF} = 7 x 10^{23} m^{-3} corresponding to a 1% NF volume fraction was used in all cases. In all the NFA models the NFs, are the highest density sink with a strength of ≈ 10^{16} m^{-2}. The NF play a significant role in collecting He. Up to ≈ 10^{-4} dpa the NFs collect ≈ 100 % of the He, but at this point the He is mostly in the form of single atoms that are loosely bound and are emitted back to the matrix at a rate dictated by the binding energy of E_{bnf} = 0.6 eV. The corresponding matrix He(s) and He(i) build up to the peak values of ≈ 10^{-9} and 10^{-21}, respectively, balancing the emission of trapped He from the NFs. The matrix He continues to flow to dislocations, matrix bubbles and GB subregions. Accelerated He collection starts once bubble formation becomes significant in these regions. Dislocations become the primary He collector around 10^{-3} dpa after both homogeneous and heterogeneous bubble nucleation have begun as shown in Figure 5d. Helium build-up in the other features slows down, and dislocations continue to collect most of the He up to ≈ 1 dpa. He bubbles start forming on NFs, which leads to accelerated He partitioning to that region around 0.01 dpa. He partitioning to NF catches up to dislocations at ≈ 10 dpa. Helium partitioning to matrix bubbles is low (≈ 10^{-3} of the total He) because the other microstructural features more effectively collect He. Helium partitioning to GB is strongly affected by grain size, so that in the 2μm grain size case partioning to GBs is ≈ 3 x 10^{-5} of the total He, which is ≈ 10^{3} times more than for the 20μm grain size model. The resulting GB He coverage is ≈ 2 x 10^{-5} and the average GB bubble radius is ≈ 0.25 nm. This suggests such a small, subvisible He bubbles in exist every ≈ 2x10^{4} nm^{2}.

Figure 9 shows the number density and radius of He bubbles formed in various sub-regions as a function of dpa. At 10 dpa, ≈ 72% of the total bubbles formed on dislocations homogeneously as well as at trap sites that include dislocation intersections and NFs trapped on dislocations. About, ≈ 27% of the bubbles formed on NFs in the matrix, and ≈ 1% of the bubbles formed homogeneously in the matrix. A further break down for the dislocation bubbles are: ≈ 52% as homogeneous; ≈ 12% on NFs; and ≈ 8% at intersections. Both NFs in the matrix and on dislocations assisted are sites for ≈ 39 % of the bubble formation. Due to the high dislocation and the NF number densities, the He bubble number density was ≈ 4 x 10^{23} m^{-3} and the average bubble radius was ≈ 0.6 nm. The results for the NFA models are in very good agreement with the results obtained from the He implanter experiments.

Bubble Size Distribution

Figure 10a shows the bubble size distributions obtained from a TMS model with ρ = 10^{15} m^{-2} and d_g = 20 μm. The figure also shows experimental results for F82H mod.3 in the AT and 20%CW conditions. The microstructural parameters in this model better correspond to the 20%CW case. The results give only a single mode distribution since the current model does not include bubble to void transformation, whereas the experimental results shows a bimodal distribution with a lower number of larger voids. Nevertheless, the agreement of the model with the bubble part of the experimental results in the 20%CW case is excellent. Note that, the experimental TEM observations are only valid for bubbles larger than ~1 nm in diameter. Figure 10b shows the corresponding bubble distribution comparison for the NFA model with ρ = 10^{15} m^{-2} and d_g = 2 μm and the experimental results for NFA MA957 and 12YWT at the corresponding condition. With no bubble to void transformation observed in these alloys, the model shows even better agreement with experiment.

First Order Estimates of Void Growth in the TMS model

While the current model does not include an algorism to deal with bubble-to-void transformation, the experimental bubble distribution shown in Figure 10a, after 5 dpa of irradiation, includes a population of large bubbles exceeding the critical size, which assures their continued growth by absorbing excess vacancies. The large bubbles were manually separated from the distribution obtained at 1 dpa, and

grown as voids at a rate dictated by the excess vacancy flux in the model. Figure 11 shows the results of the void growth and estimation of swelling of the F82H mod.3 steel. This result suggests that a few percent swelling may occur in a TMS steel at 100 dpa with the assistance of He. Future models will directly incorporate the critical bubble void nucleation and growth.

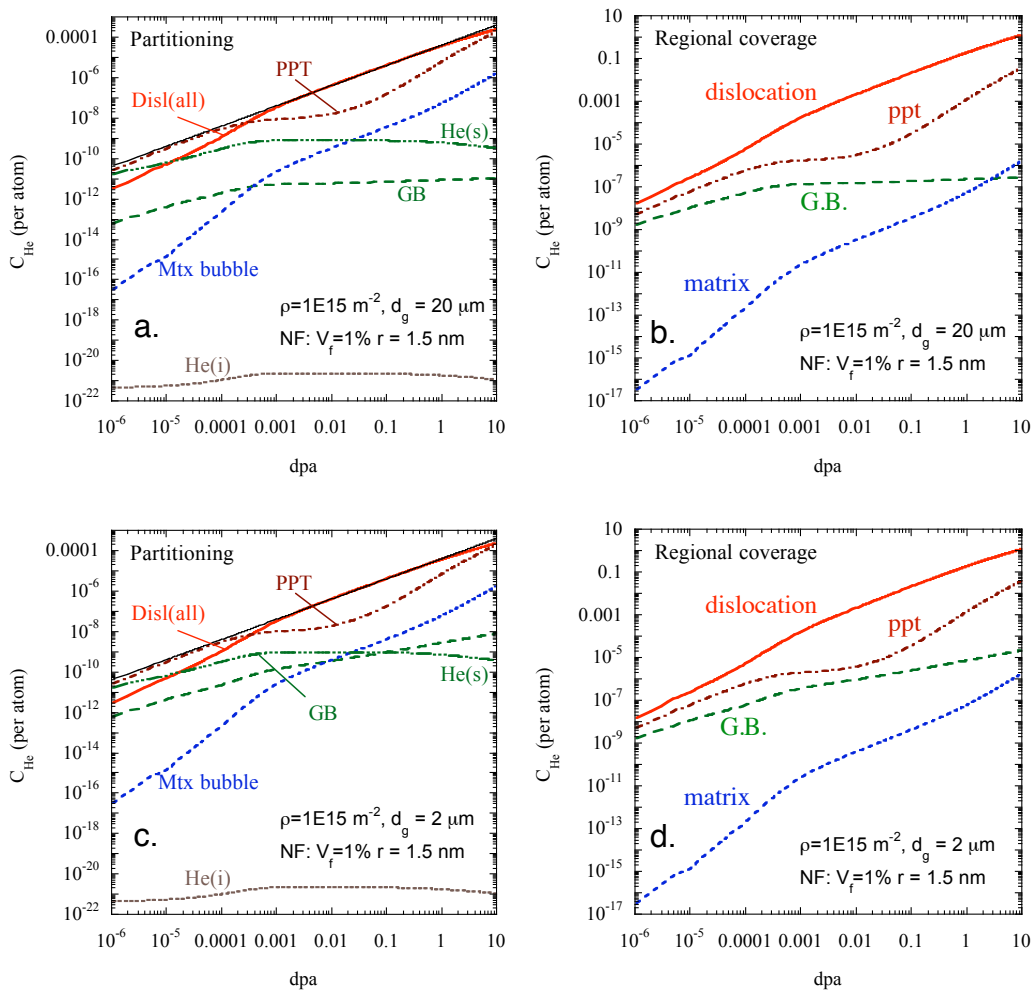

Figure 8 He partitioning and He coverage of subregions for NFA models with two grain sizes, d_g = 20 μm (a, b) and d_g = 2 μm (c,d).

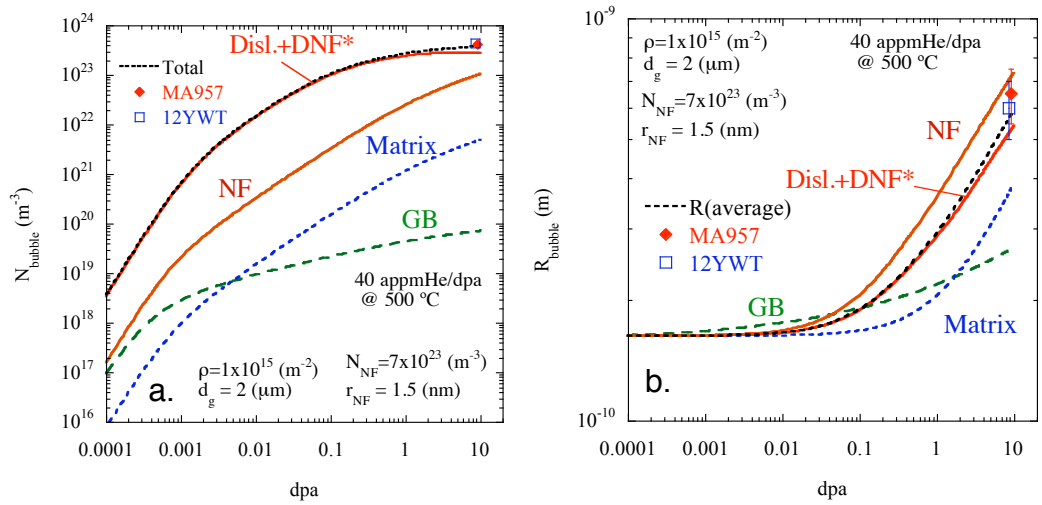

Figure 9 Number density and size of He bubbles in the NFA model with grain size of d_g = 2μm, compared with the observation in He-implanter experiments on two NFAs, MA957 and 12YWT.

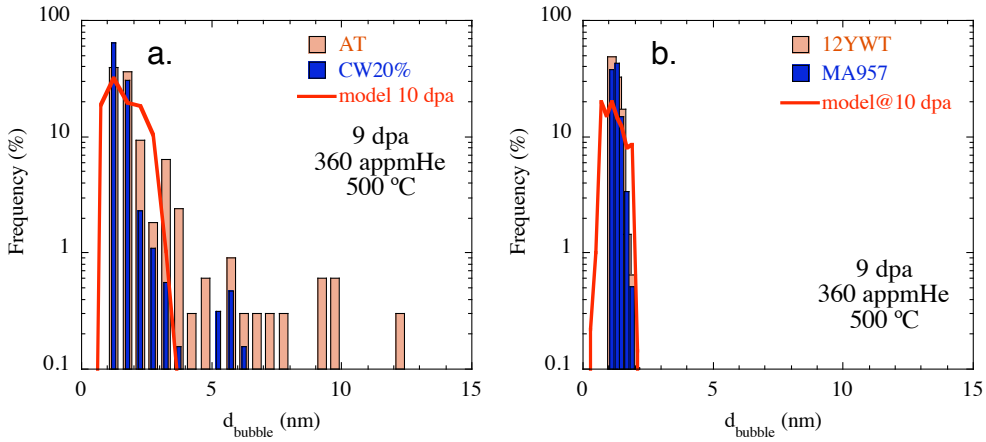

Figure 10 Bubble size distributions by TMS and NFA models with experimental observations in comparable alloy and irradiation conditions.

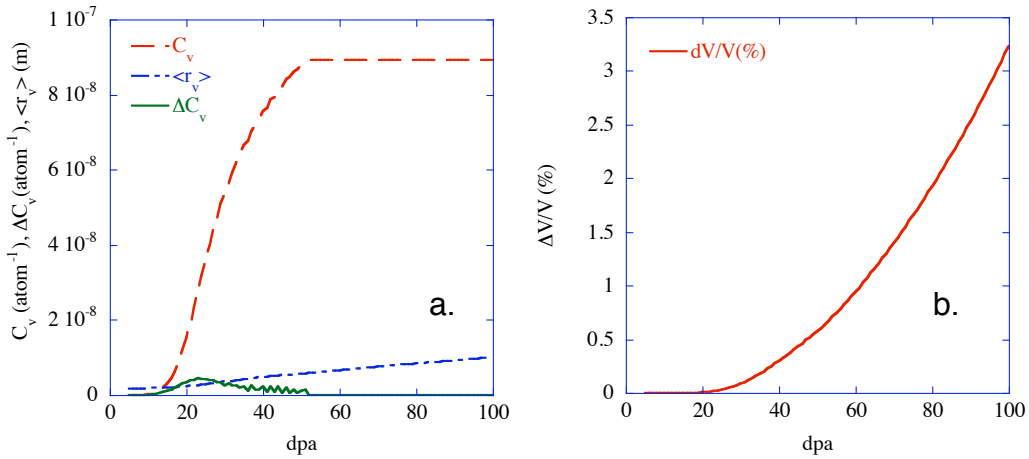

Figure 11 First order estimates of void growth in the TMS model with $\rho=10^{15}$ m^{-2} and d_g = 2 μm; (a) void number density, C_v, nucleation, ΔC_v, and average radius, $<r_v>$, and (b) swelling as a function of dpa.

Future Research

Refinement of the model to treat lath boundaries and to integrate bubble to void conversion and void growth models will be carried out during the current reporting period.

References

1. Y. Dai, G. R. Odettte, T. Yamamoto, *The Effects of helium on irradiated structural alloys (2011) in press.*
2. T. Yamamoto, G.R. Odette, H. Kishimoto, J-W. Rensman, P. Miao, *J. Nucl. Mater.* **356** (2006) 27.
3. G.R. Odette, T. Yamamoto, H.J. Rathbun, M.Y. He, M.L. Hribernik, J.W. Rensman*, J. Nucl. Mater.* **323** (2003) 313.
4. T. Yamamoto, Y. Dai, G. R. Odette, M. Salston, P. Miao, *Trans. American Nuclear Society,* 98 (2008) 1111.
5. T. Yamamoto, G.R. Odette, P. Miao, D. T. Hoelzer, J. Bentley, N. Hashimoto, H. Tanigawa, R. J. Kurtz, J. Nucl. Mater. 367 (2007) 399.
6. G.R. Odette, M.J. Alinger, and B.D.Wirth, Annu. Rev. Mater. Res. 38 (2008)471.
7. G.R. Odette, P. Miao, D.J. Edwards, T. Yamamoto, R. J. Kurtz, Y. Tanigawa, J. Nucl. Mat. (2010) in press.
8. B.D. Wirth, G.R. Odette, J Marian et al., J. Nucl. Mater. 329-333 (2004) 103
9. R.J. Kurtz and H. L. Heinisch, J. Nucl. Mater. 329-333 (2004) 1199-1203.
10. R.J. Kurtz, H.L. Heinish and F. Gao, J. Nucl. Mater. 382 (2008) 134.
11. H. L. Heinisch, F. Gao, R.J. Kurtz, E. A. Le, J. Nucl. Mater. 351 (2006) p141-148.
12. H. L. Heinisch, F. Gao, R.J. Kurtz, Phil. Mag. 90 (2010) 885.
13. F. Gao, H. L. Heinisch, R. J. Kurtz, J. Nucl. Mater. 351(2006) 133-140.
14. F. Gao, H. L. Heinisch, R. J. Kurtz, J. Nucl. Mater. 367-370(2007) 446-450.
15. F. Gao, H. L. Heinisch, R. J. Kurtz, J. Nucl. Mater. 386-388 (2009) 390-394.

16. L. Ventelon, B. Wirth, C. Domain, J. Nucl. Mater. 351 (2006) 119–132.
17. Jae-Hyeok Shim, Sang Chul Kwon, Whung Whoe Kim, Brian D. Wirth, J. Nucl. Mater. 367-370 (2007) 292-297.
18. R.E. Stoller, G.R. Odette, J. Nucl. Mater. 131 (1985) 118.
19. C. C. Fu, F. Willaime, Phys Rev. B 72, 064117(2005).
20. K. Morishita, R. Sugano, B.D. Wirth, T. D. de la Rubia, Nuclear Instruments and Method s in Physics Research B 202 (2003) 76–81.
21. T. Yamamoto, G. R. Odette, L. R. Greenwood, *Fusion Materials Semiannual Report 1/1 to 6/30/2005* DOE/ER-313/38 (2005) 95.
22. R.J. Kurtz, G.R. Odette, T. Yamamoto, D.S. Gelles, P. Miao, B.M. Oliver, *J. Nucl. Mater.* 367-370, 417 (2007).
23. T. Yamamoto, G.R. Odette, P. Miao, et al., J. Nucl. Mater. 386-388 (2009) 338.